Flow characterization and dilution effects of N_2 and CO_2 on premixed CH_4/air flames in a swirl-stabilized combustor*

Han Yue(韩 乐)[a)†], Cai Guo-Biao(蔡国飙)[a)], Wang Hai-Xing(王海兴)[a)], Renou Bruno[b)], and Boukhalfa Abdelkrim[b)]

[a)] *School of Astronautics, Beijing University of Aeronautics and Astronautics, Beijing* 100191, *China*
[b)] *UMR* 6614 *CORIA, INSA de Rouen, Avenue de l'Université, BP* 08, 76801 *Saint-Etienne du Rouvray, France*

(Received 21 October 2013; revised manuscript received 26 December 2013; published online 12 February 2014)

Numerically-aided experimental studies are conducted on a swirl-stabilized combustor to investigate the dilution effects on flame stability, flame structure, and pollutant emissions of premixed CH_4/air flames. Our goal is to provide a systematic assessment on combustion characteristics in diluted regimes for its application to environmentally-friendly approaches such as biogas combustion and exhaust-gas recirculation technology. Two main diluting species, N_2 and CO_2, are tested at various dilution rates. The results obtained by means of optical diagnostics show that five main flame regimes can be observed for N_2-diluted flames by changing excess air and dilution rate. CO_2-diluted flames follow the same pattern evolution except that all the domains are shifted to lower excess air. Both N_2 and CO_2 dilution affect the lean blow-out (LBO) limits negatively. This behavior can be counter-balanced by reactant preheating which is able to broaden the flammability domain of the diluted flames. Flame reactivity is degraded by increasing dilution rate. Meanwhile, flames are thickened in the presence of both diluting species. NO_x emissions are significantly reduced with dilution and proved to be relevant to flame stability diagrams: slight augmentation in NO_x emission profiles is related to transitional flame states where instability occurs. Although dilution results in increase in CO emissions at certain levels, optimal dilution rates can still be proposed to achieve an ideal compromise.

Keywords: dilution effect, premixed combustion, swirl flow, optical diagnostics

PACS: 47.70.Pq, 47.70.Fw, 47.50.Ef, 47.27.ep **DOI:** 10.1088/1674-1056/23/3/034704

1. Introduction

Recent years have witnessed a worldwide increasing discussion on energy and environmental issues. Efforts have been directed towards fossil fuel saving and environment protection, giving birth to a new generation of technologies. Meanwhile, replacement of limited fossil fuel with renewable energy source, such as biomass fuel and natural gas, is of great interest in order to keep pace with the rapid growth in the global demand for energy. At the same time, more and more stringent ecological constraints concerning pollutant emissions have been imposed by both local regulations and international agreements such as the famous Kyoto protocol. In this regard, not only carbon dioxide and other greenhouse effect gas emissions, but also NO_x emissions that are responsible for air pollution have to be reduced. Hence, it is expected that environmentally-friendly combustion procedures would be developed.

Research driven by this dual challenge covers a wide scope of real-world applications. Based on lean premixed combustion, great progress has been made in the clean combustion of biogas through the use of dry low emission technologies. Biogas is a renewable energy source that is composed primarily of methane, along with such minor species as carbon dioxide and nitrogen. In automotive industry, a growing interest in exhaust gas recirculation (EGR) of internal combustion engines as a viable solution to clean combustion has emerged in the past decades. It is achieved by recirculating hot exhaust gases, which is mainly carbon dioxide and nitrogen, in the fresh reactants. Thus, it can be concluded that, either for the purpose of studying the biogas combustion, or for investigating the combustion performance in diluted regimes motivated by the EGR technology, it is reasonable to consider N_2 and CO_2 as two major diluents that can be added into reactant mixtures. This is the motivating factor for choosing N_2 and CO_2 as representative diluents in our experiments on the diluted methane/air flames.

Depending on the diluent characteristics, dilution leads to modification in the thermophysical properties and could also affect the elementary chemical reactions. On the other hand, the dilution of fresh gases influences the flame reactivity, which can induce stability problems. Thus, it is of paramount importance to enhance the knowledge about typical diluents, especially their impacts on the behavior of the diluted combustion regime. The fundamental research on diluted combustion with or without air preheating is not a new topic. It can be traced back to the last century when non-premixed diluted flames in both counter-flow and co-flow configurations have been extensively investigated. Among those studies, the flame characteristics, such as flammability limits,[1,2] flame stability,[3] flame structure,[3–5] flame temperature uniformity,[6] and NO_x emission[6,7] have been analyzed under various diluted combustion conditions. Such studies benefit from the existing database of diffusion flames since simple reference flames can easily be found to compare

*Project supported by the China Scholarship Council.
†Corresponding author. E-mail: hanyue@sa.buaa.edu.cn
© 2014 Chinese Physical Society and IOP Publishing Ltd

with. Another advantage of those experimental configurations is that it is more conveniently accessible to laser diagnostics. In the counterpart, fewer results have been reported concerning the premixed or partially premixed diluted flames. Feasibility studies were conducted in a first stage to provide guidelines for burner design.[8] Galmiche *et al.*[9] reported an interesting fundamental study in which laminar burning velocities were determined for a large set of diluents (nitrogen, carbon dioxide, water vapor, a mixture of these three previous gases, helium and argon) and for different dilution levels. Considering that heat capacity seems to possess the predominant effect on the laminar flame, an explicit correlation between the heat capacity of the diluents and the laminar burning velocity was proposed, allowing the prediction of the laminar burning velocity, regardless of the diluents and the dilution levels. So far, few prior studies have systematically examined the effect of nitrogen and carbon dioxide on premixed methane/air flame properties.

We aim to evaluate the effects of the main diluting species (N_2 and CO_2) on methane/air flames in swirl-stabilized configuration under lean premixed combustion conditions through experiments and numerical simulations. This paper is organized as follows. Section 2 introduces the model combustor and the instrumentation used to carry out optical diagnostics and other measurements, and presents numerical implementations for both non-reacting and reacting flows. Visualization and characterization of non-reacting swirling flows are provided in Section 3. Dilution effects on combustion stability are detailed in Section 4 through the results of CH* chemiluminescence measurements. Dilution effects on flame structure are described in Section 5 with the help of planar laser-induced fluorescence on OH radical (OH-PLIF) measurements and Chemkin calculations. Dilution effects on pollutant emissions are discussed in Section 6. Concluding remarks are summarized in Section 7.

2. Experimental and numerical methods

2.1. Experimental setup

The fundamental experimental setup employed in this work is composed of multiple components and subsystems, as shown in Fig. 1. Air, N_2, and CO_2 streams are separately controlled by mass flow meters (Bronkhorst EL-FLOW Select) that are properly calibrated. N_2-diluted or CO_2-diluted air mixture is then delivered by a gas mixer commercially available. Since preheating impacts are planned to be discussed, the diluted air passes through a homemade gas heater downstream the gas mixer. Considering the heat losses through the pipelines, a thermocouple (T_1) is placed at the exit of the electric heater, while another one (T_2) is located at the entry of swirl injector. The gas heater receives temperature signals from the thermocouple T_2 and automatically adjusts the temperature setpoint (T_1) with the help of a feedback circuit, until that the temperature measured by the thermocouple T_2 attains the expected preheating temperature. For safety concerns, only the diluted air is preheated by means of the electric heater. In order to achieve completely premixed conditions, a homemade fuel–air mixer is employed upstream of the swirl injector. The counter flow configuration of the mixer is proved to promote the mixing process in our application. A Labview interface is developed to globally control the gas supply system according to the desired operating conditions.

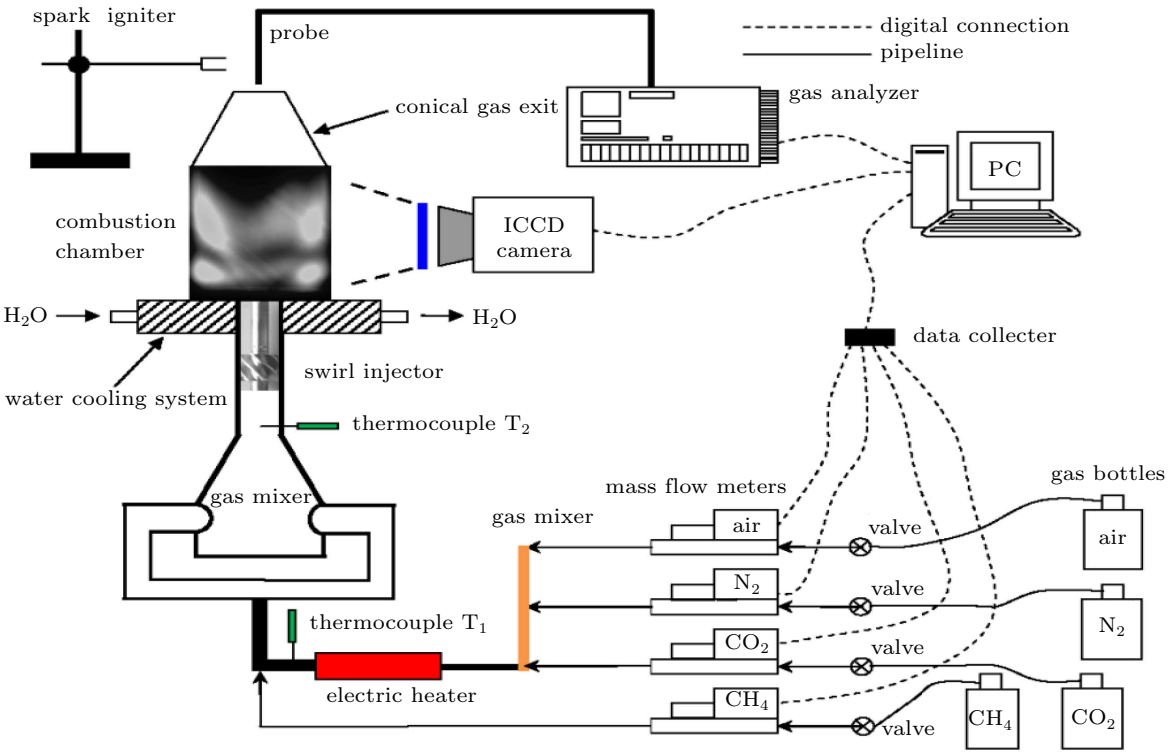


Fig. 1. (color online) Schematic diagram of experimental arrangements.

It is anticipated that challenges to lean premixed burner design is two-fold: achieving acceptable flame stability and maintaining stability with varying fuel composition. As a predominant flow mechanism found both in premixed and non-premixed practical combustion systems, swirl provides an effective means to control flame stability as well as the combustion intensity.[10–14] For premixed combustion, the recirculation zone generated by the sufficiently intense swirling motion plays an important role in the flame stabilization process, as it retains a steady supply of radicals and hot combustion products to continuously ignite the fresh reactants. Flame stabilization also benefits from the generation of a compact swirling flame with much higher combustion intensity than in a non-swirling case. With reference to an extensive review given by Syred and Beér[13] on the topic of the basic processes and practical implementation of swirl combustors, a swirl-stabilized combustor is designed for the present study. An axial swirl injector of 18-mm outer diameter is mounted on the base of the combustion chamber. The injector comprising six helical vanes with a 50° angle to the flow axis surrounded a center body of 10 mm diameter (Fig. 2). The geometry-based swirl number[12] is estimated to be 0.952. Premixed air and fuel flows pass through angled vanes before they are injected to the combustion chamber.

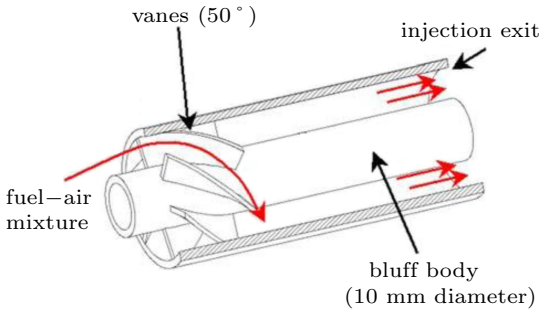


Fig. 2. (color online) Schematic of swirl injector.

The combustion chamber is equipped with a cylindrical quartz tube (Herasil) with an internal diameter of 80 mm, a height of 200 mm, and a thickness of 5 mm. The polished surface of the quartz tube is of high quality, providing full optical access to allow optical diagnostics. A conical gas outlet is installed at the top of the tube as the exhaust port of the combustion chamber, so that the combustor operates at ambient pressure. The flame ignition is achieved by a spark igniter situated at the chamber exit. A water-cooling system is fixed on the base to limit the strain of temperature.

Exhaust gas composition downstream the dilution air injection are obtained from a five-gas analyzer HORIBA 1500. NO_x emissions are measured by a chemiluminescence sensor, and CO emissions are detected by a non-dispersive infrared (NDIR) sensor. The gas analyzer probe is located close to the gas exit.

2.2. Large eddy simulations (LES) for non-reacting flows

2.2.1. Governing equations and sub-grid scale (SGS) modeling

Navier–Stokes equations are filtered in order to perform large eddy simulations for non-reacting flows. The complete Favre-averaged formulations for mass, momentum, energy, and species concentration are written as

$$\frac{\partial \overline{\rho}}{\partial t} + \frac{\partial \overline{\rho}\widetilde{u_i}}{\partial x_i} = 0, \tag{1}$$

$$\frac{\partial \overline{\rho}\widetilde{u_i}}{\partial t} + \frac{\partial(\overline{\rho}\widetilde{u_i}\widetilde{u_j} + \overline{p}\delta_{ij})}{\partial x_j} = \frac{\partial(\widetilde{\tau}_{ij} - \tau_{ij}^{\mathrm{sgs}})}{\partial x_j}, \tag{2}$$

$$\frac{\partial \overline{\rho}\widetilde{E}}{\partial t} + \frac{\partial[(\overline{\rho}\widetilde{E} + \overline{p})\widetilde{u_i}]}{\partial x_i} = -\frac{\partial}{\partial x_i}\left(\widetilde{u_j}\widetilde{\tau_{ij}} + \lambda\frac{\partial \widetilde{T}}{\partial x_i} - H_i^{\mathrm{sgs}} + \sigma_i^{\mathrm{sgs}}\right), \tag{3}$$

$$\frac{\partial \overline{\rho}\widetilde{Y_k}}{\partial t} + \frac{\partial(\overline{\rho}\widetilde{Y_k}\widetilde{u_j})}{\partial x_j} = \overline{\dot{\omega}_k} + \frac{\partial}{\partial x_j}(\overline{\rho}\widetilde{U}_{k,j}\widetilde{Y_k} - \Phi_{k,j}^{\mathrm{sgs}} - \Theta_{k,j}^{\mathrm{sgs}}), \tag{4}$$

where i is the spatial coordinate index, j is the dummy index to spatial coordinate, k is the species index, ρ is the density, u is the velocity component, E is the total energy, T is the temperature, p is the pressure, τ_{ij} is the viscous stress tensor, Y_k is the mass fraction of species k, $U_{k,j}$ is the diffusion velocity of species k, λ is the thermal conductivity, and $\dot{\omega}_k$ is the species mass production rate.

The unclosed sub-grid scale (SGS) terms are defined as

$$\tau_{ij}^{\mathrm{sgs}} = \overline{\rho u_i u_j} - \overline{\rho}\widetilde{u_i}\widetilde{u_j}, \tag{5}$$

$$H_i^{\mathrm{sgs}} = (\overline{\rho E u_i} - \overline{\rho}\widetilde{E}\widetilde{u_i}) + (\overline{p u_i} - \overline{p}\widetilde{u_i}), \tag{6}$$

$$\sigma_{ij}^{\mathrm{sgs}} = \overline{u_j \tau_{ij}} - \widetilde{u_j}\widetilde{\tau_{ij}}, \tag{7}$$

$$\Phi_{k,j}^{\mathrm{sgs}} = (\overline{\rho Y_k u_j} - \overline{\rho}\widetilde{Y_k}\widetilde{u_j}), \tag{8}$$

$$\Theta_{k,j}^{\mathrm{sgs}} = (\overline{\rho Y_k U_{k,j}} - \overline{\rho}\widetilde{Y_k}\widetilde{U_{k,j}}), \tag{9}$$

where τ_{ij}^{sgs} is the SGS stress term, H_i^{sgs} is the SGS energy flux term, $\sigma_{ij}^{\mathrm{sgs}}$ is the SGS viscous work term, $\Phi_{k,j}^{\mathrm{sgs}}$ is the SGS species flux term, and $\Theta_{ij}^{\mathrm{sgs}}$ is the SGS species diffusive flux term.

Most of the SGS models are based on an eddy-viscosity type model. The sub-grid stress is associated with the large-scale strain-rate tensor $\widetilde{S_{ij}}$

$$\tau_{ij}^{\mathrm{sgs}} = 2\nu_t\widetilde{S_{ij}} + \frac{\delta_{ij}}{3}\tau_{kk}^{\mathrm{sgs}}, \tag{10}$$

where ν_t is the sub-grid eddy viscosity, and

$$\widetilde{S_{ij}} = \frac{1}{2}\left(\frac{\partial u_j}{\partial x_i} + \frac{\partial u_i}{\partial x_j}\right). \tag{11}$$

Based on the local equilibrium hypothesis, algebraic Smagorinsky model is applicable

$$\nu_t = (C_{\mathrm{S}}\Delta)^2|\widetilde{S}|, \tag{12}$$

where Δ is the filter width, and $|\widetilde{S}| = (2\widetilde{S}_{ij}\widetilde{S}_{ij})^{1/2}$. The coefficient C_s can be determined by the isotropic turbulence decay.

Erlebacher *et al.*[15] extended the above model by taking into account the effects of flow compressibility, which yields

$$\tau_{ij}^{\rm sgs} = -2\nu_t\overline{\rho}\left(\widetilde{S}_{ij} - \frac{\widetilde{S}_{kk}\delta_{ij}}{3}\right) + \frac{2}{3}\overline{\rho}k^{\rm sgs}\delta_{ij}, \quad (13)$$

$$\nu_t = C_{\rm R}(\Delta D)^2|\widetilde{S}|, \quad (14)$$

$$k^{\rm sgs} = C_{\rm I}(\Delta D)^2\widetilde{S}_{ij}\widetilde{S}_{ij}. \quad (15)$$

The dimensionless coefficients C_R and C_I are two parameters of the compressible Smagorinsky model. The Van-Driest damping function D is applied to account for the inhomogeneities near the surface[16] and expressed as

$$D = 1 - \exp(1 - (y^+)^3/26^3), \quad (16)$$

$$y^+ = \frac{yu_\tau}{\nu}, \quad (17)$$

where u_τ is the friction velocity.

The calculation of the sub-grid energy flux term is achieved by adopting the following expression:

$$H_i^{\rm sgs} = -\overline{\rho}\frac{\nu_t}{{\rm Pr_t}}\frac{\partial\widetilde{H}}{\partial x_i} = -\overline{\rho}\frac{\nu_t}{{\rm Pr_t}}\left(\frac{\partial\widetilde{h}}{\partial x_i} + \widetilde{u}_j\frac{\partial\widetilde{u_j}}{\partial x_i} + \frac{1}{2}\frac{\partial k^{\rm sgs}}{\partial x_i}\right). \quad (18)$$

The turbulent Prandtl number Pr_t is set to 0.7.

The sub-grid convective species term is approximated as

$$\Phi_{k,j}^{\rm sgs} = -\overline{\rho}\frac{\nu_t}{{\rm Sc_t}}\frac{\partial\widetilde{Y}_k}{\partial x_i}, \quad (19)$$

where Sc_t is the turbulent Schmidt number.

The SGS viscosity work term $\sigma_{ij}^{\rm sgs}$ and the SGS species diffusive fluxes term $\Theta_{k,j}^{\rm sgs}$ are both negligible considering their minor contribution to the total energy.

2.2.2. Numerical implementation

Density-based finite volume method is adopted, with dual-time stepping integrations, to solve the above described Navier–Stokes equations with adequate sub-grid modeling. In detail, third-order total variation diminishing (TVD) scheme is applied to convective terms; second-order central difference scheme is used in viscous terms; physical time step is calculated by second-order back difference scheme; virtual time step is carried out by the fourth-order Runge–Kutta scheme. In all cases, second-order accurate boundary conditions are implemented. Inlet and outlet conditions are specified using characteristic boundary conditions. Inviscid and adiabatic conditions are imposed at solid wall.[17] Other conditions are specified using second-order extrapolated values, leading to zero normal gradients with respect to pressure, velocity, temperature, and species mass fraction.

2.3. Chemkin calculations for reacting flows

In order to evaluate flame structure, adiabatic laminar flame speed S_L^0 is computed with Chemkin code. The standard version of Chemkin code deals with the determination of one-dimensional flame characteristics by solving steady ODEs of Navier–Stokes equations. Concerning the closure of the equations, a multi-component transport model introduced by Dixon-Lewis[18] is chosen to evaluate the transport property; a kinetic mechanism from the GRI-Mech 3.0 data is used,[19] which involves 53 species and 325 reactions. In this study, laminar flame speeds for different fuel mixture and the related temperature distribution are obtained by Chemkin calculations.

2.4. Optical diagnostics for reacting flows

2.4.1. CH* chemiluminescence

Chemiluminescence of CH* radicals[20] is carried out by an intensified CCD camera (Princeton, 512×512 pixels) coupled with a Nikkor lens (50 mm, $f/1.8$) in order to observe reaction intensity and flame location in the combustion chamber. A narrow band pass filter (Schott BG12) centered at 431 nm allows the detection of CH* radicals. For each operating condition, 300 instantaneous flame images have been recorded consecutively (frequency = 10 Hz). Exposure time is set to 2 ms while the gain is adjusted to 100 based on the case corresponding to maximum level of collected CH* signal. These two parameters are kept constant during all the measurements so that the results from different experimental conditions are comparable. Average and RMS images are also calculated so as to characterize different combustion regimes.

2.4.2. OH-PLIF

In planar laser-induced fluorescence on OH radicals (OH-PLIF) imaging, transient locations of the reaction zones are identified by OH radical distributions. Figure 3 describes the experimental setup of OH-PLIF measurements performed in this study. To induce fluorescence in OH radicals, a laser system consisting of an Nd:YAG laser (Spectra Physics, Quanta Ray) and a tunable dye laser (Sirah Precision Scan) is employed. High-intensity pulse (450 mJ per pulse) is efficiently frequency-doubled in the Nd:YAG laser to generate laser beam at 532 nm, which is used to pump the dye laser operating with Rhodamine 6 G dissolved in methanol solvent. The resultant doubled beam is tuned to a wavelength of about 282.66 nm. At the exit of the dye laser, the generated laser pulse is measured to be around 20 mJ of energy per shot, with a pulse width of 10 ns. In this experiment, the $Q_1(5)$ transition in the $A^2\Sigma^+ < -X^2\Pi_i$ ($v' = 1 < -v'' = 0$) band of OH radical is excited and fluorescence from the A-X(1,0) and (0,0) bands (wavelength: 306–320 nm) can be collected. The laser beam

is then shaped into a thin vertical sheet after passing through a series of sheet-forming optics. The present optical arrangement is composed of a UV fused silica plano-convex lens ($f = 1000$ mm), a divergent cylindrical lens ($f = -200$ mm) and a spherical lens ($f = 100$ mm). The cylindrical lens and the spherical lens are served to control the height (~ 56 mm) and the thickness (~ 200 μm) of the laser sheet, respectively. Thereupon, the created and optimized laser sheet is introduced into the measurement section in order that a spatial map of OH signals can be acquired and recorded with the help of a detection system. In detail, two-dimensional OH fluorescence signals are collected with a UV Nikkor lens (105 mm, $f/4.5$) and focused onto a 16-bit intensified CCD camera (Princeton PI-MAX, 512×512 pixels) in the direction orthogonal to the laser sheet. The ICCD camera is operated with a gating time of 100 ns, and fitted with a combination of WG305 and UG11 filters (Schott glass) so as to reject the undesirable UV wavelength and avoid detection of flame luminosity and spurious light scattering. In general, the PLIF system affords a field of view of 42.6 mm $\times$ 42.6 mm. To provide a sound basis for analysis, 300 single-shot OH distributions are taken for each experimental flame condition. Triggering and synchronization of the lasers with the ICCD camera is ensured by a digital delay/pulse generator (BNC, model 575).

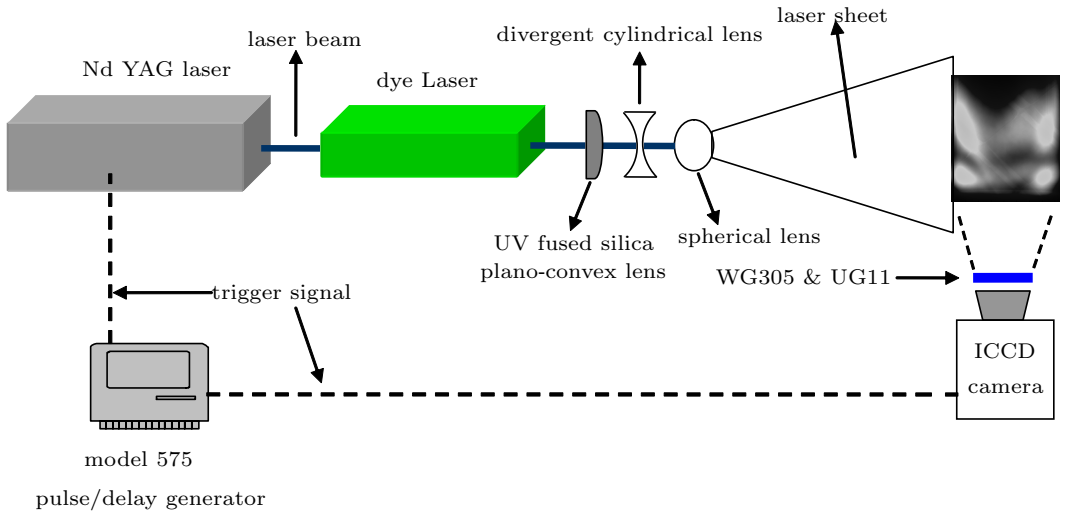


Fig. 3. (color online) Experimental setup of OH-PLIF system.

2.4.3. Plane of measurement

CH* chemiluminescence imaging is performed to establish flame stability maps in order to put in evidence the different flame regimes. Accordingly, the field of view is set to an appropriate size (90 mm $\times$ 90 mm), large enough to enable the visualization of the primary reaction zones, while not large enough to maintain a good image resolution (5.7 pixels/mm). By contrast, OH-PLIF measurements are served to explore detailed flame structures so that spatially resolved local information is essentially required. An image scaling of 12.1 pixels per mm is obtained by limiting the total imaging area to 42.6 mm $\times$ 42.6 mm.

Flames confined in the cylinder tube are considered to be axisymmetric, so the median plane is chosen as the plane of measurement for OH-PLIF. This plane of measurement is delicately positioned as shown in Fig. 4. Due to the global symmetry, only the right half of the swirling flame is captured. A slight shift to the left of the centerline is intentionally adjusted, with the goal of observing the whole injection section. Another benefit of this subtle modification is to avoid tube wall interference, thus improving image quality. The lower edge of the raw OH-PLIF images is approximately 2 mm downstream the exit plane of the swirl injector. Under some operating conditions, corner recirculation zones are expected to appear. With the current positioning strategy, the existence of such recirculation zones can be identified.

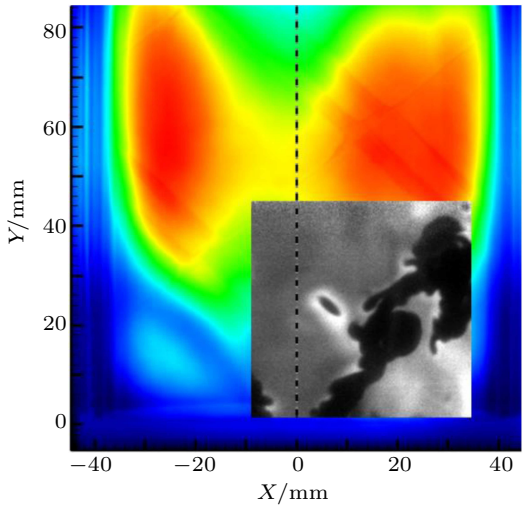


Fig. 4. (color online) Comparison of planes of measurements (colored image: averaged flame obtained by CH* chemiluminescence; black-and-white image: instantaneous flame obtained by OH-PLIF; dashed line: centerline of the combustion chamber).

3. Non-reacting flow characterization

The importance of non-reacting flow characterization is two-fold. On the one hand, quantitative information about the velocity field allows us to determine the aerodynamic swirl number, which serves to explain the observed recirculation zones. On the other hand, knowledge on cold flow topology is essential to validate the design of the swirl injector in this study. This first step is indispensible to guarantee the appropriate performance of the swirl-stabilized combustor under combustion conditions.

For this purpose, LES simulations are performed at atmospheric pressure (1 atm). The temperature is fixed at 300 K. Even if the main flow topology obtained in the cold flow will be slightly modified by heat release as the internal recirculation zone weakens, it is of interest to present the mean flow properties within the combustion chamber. The computational domain downstream of the injector measures a length of 60 mm and a radius of 30 mm, with an axisymmetric configuration. The entire grid system consists 200×125 points along the axial and radial directions, respectively. The mesh size in the radial direction varies progressively so that local refinement is achieved, close to the injector. The primary air flow rate is fixed at 4.78 g/s in order to roughly achieve the same injection velocity as the operating conditions for reacting flows.

The mean velocity field obtained by LES simulation is displayed in Fig. 5. Meanwhile, radial profiles of the axial, radial and azimuthal velocity components at different axial locations are extracted and plotted in Figs. 6–8. According to Fig. 5, the swirl flow can be characterized by three main zones: an internal recirculation zone (IRZ), a corner recirculation zone (CRZ), and a shear layer zone.

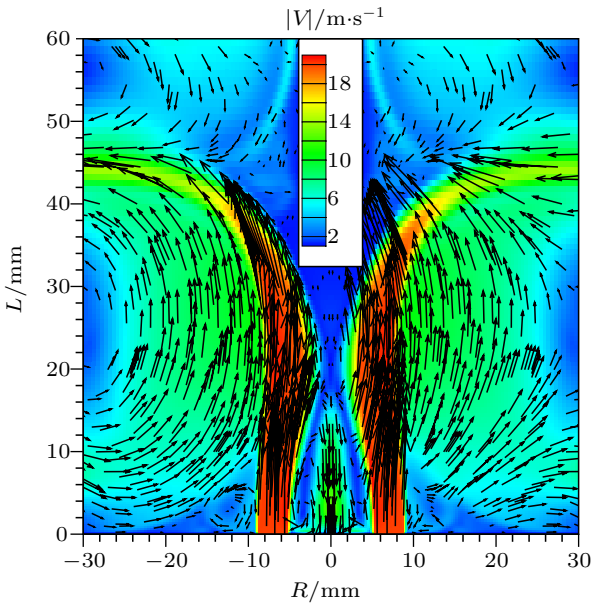


Fig. 5. (color online) Mean velocity field (R: radial direction, L: axial direction, color bar: velocity magnitude).

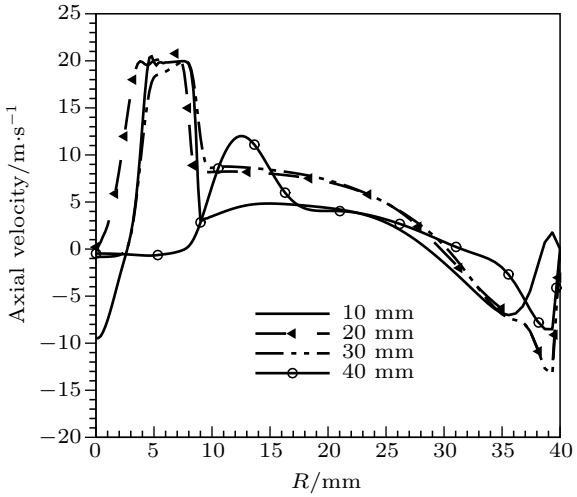


Fig. 6. Mean radial profile of axial velocity at different axial locations.

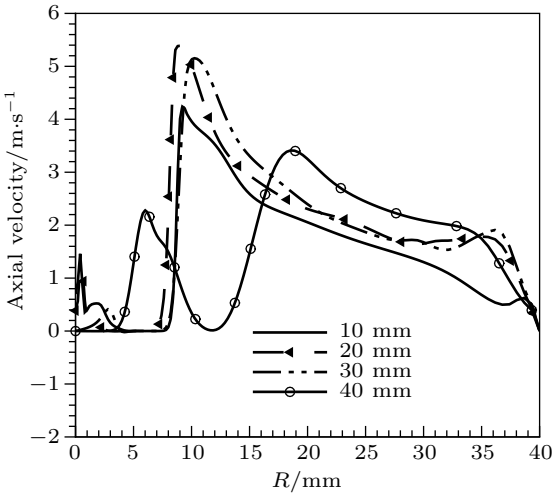


Fig. 7. Mean radial profile of azimuthal velocity at different axial locations.

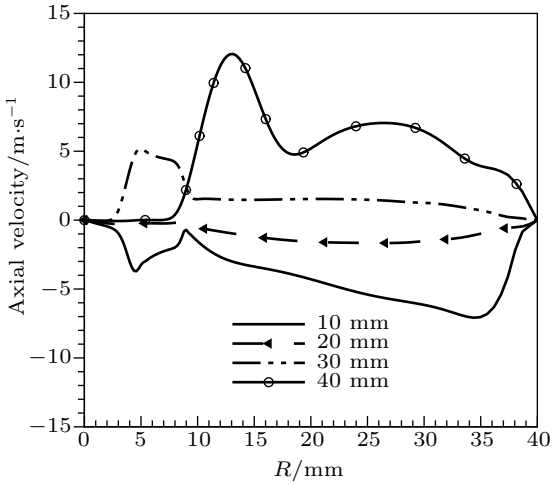


Fig. 8. Mean radial profile of radial velocity at different axial locations.

A straightforward definition of the aerodynamic swirl number is the ratio between axial flux of the swirl momentum (G_θ) and the axial flux of the axial momentum (G_z) times

the equivalent nozzle radius,

$$S = \frac{G_\theta}{G_z d/2}. \tag{20}$$

In this study, the turbulent stress term and the pressure term are neglected. Such simplification yields

$$S = \frac{\int_{R_i}^{R_0} u_z u_\theta 2\pi r^2 \mathrm{d}r}{\int_{R_i}^{R_0} \left(u_z^2 - \frac{u_\theta^2}{2}\right) 2\pi R_0 r \mathrm{d}r}. \tag{21}$$

Using this simplified expression and the velocity components given by Figs. 6–8, aerodynamic swirl numbers (S) at different locations can be estimated. For example, at 10-mm downstream the injector nozzle, $S = 0.7332$. Since for a swirl number greater than a critical value of 0.6, swirl motion can be clearly identified.[21] The obtained swirl number confirms the presence of the IRZ corresponding to axial recirculation in the form of a central toroidal recirculation zone near the injector exit. The azimuthal velocity grows linearly from the injector center until reaching a maximum before decreasing inversely proportional to the radius (Fig. 7), except for the far downstream location ($L = 40$ mm).

The appearance of a CRZ is usually caused by the sudden widening at the outlet of the injection system. The degree of widening is evaluated by a containment ratio B, defined as the ratio between the area of the flow injection and the area of the combustion chamber. For this combustor, B is estimated to be 0.035, which is much lower than the critical value ($B = 0.25$).[22] This estimation is in fully agreement with the observation of the CRZ in Fig. 5.

The intense shear layer zone is located between CRZ and IRZ and characterized by a local counter-current flow. The negative values observed in radial profiles of axial (Fig. 6) and radial (Fig. 8) velocity give evidence to the existence of IRZ, CRZ, and shear layer zones at near-injection regions ($L = 10$ mm and 20 mm).

4. Dilution effects on flame stability with or without preheating

Experimentally, N_2 and CO_2 are often separately added into fuel mixture in order to discriminate their individual impact on the combustion mechanism. The flame stability diagrams are plotted for both N_2 dilution (Fig. 9) and CO_2 dilution (Fig. 10) at 300 K. The lean blow-out (LBO) limits are determined by gradually increasing the excess air, denoted by e, for a fixed dilution level until flame extinction is achieved. It is emphasized that the measurements are limited by a maximum equivalence ratio of 0.75 (corresponding to $e = 0.333$) to ensure safety; otherwise, the temperature of the combustor wall becomes too high, which leads to explosion. The chemical reactions under consideration are listed below.

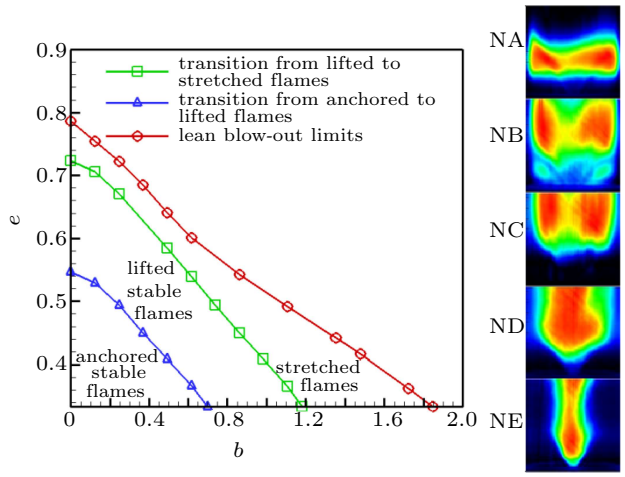


Fig. 9. (color online) Stability diagram of N_2-diluted CH_4–air flames at 300 K (e: excess air, b: dilution rate) with corresponding CH* chemiluminescence images of averaged flames (NA: anchored stable flames; NB: A–L transient unstable flames; NC: lifted stable flames; ND: L–S transient unstable flames; NE: near-extinction stretched flames).

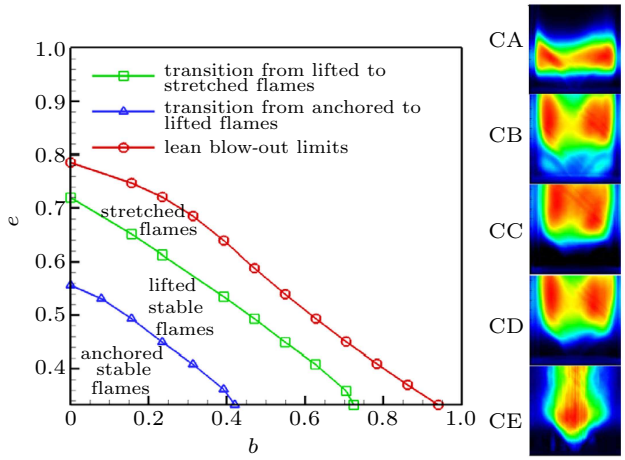


Fig. 10. (color online) Stability diagram of CO_2-diluted CH_4 air flames at 300 K with corresponding CH* chemiluminescence images of averaged flames (CA: anchored stable flames; CB: A–L transient unstable flames; CC: lifted stable flames; CD: L–S transient unstable flames; CE: near-extinction stretched flames).

N_2 dilution:

$$\begin{aligned} &CH_4 + 2(1+e)(O_2 + 3.78N_2 + bN_2) \\ &= CO_2 + 2H_2O + 2(1+e)(3.78+b)N_2 + 2eO_2, \end{aligned}$$

CO_2 dilution:

$$\begin{aligned} &CH_4 + 2(1+e)(O_2 + 3.78N_2 + bCO_2) \\ &= (1+2b(1+e))CO_2 + 2H_2O + 7.56(1+e)N_2 + 2eO_2, \end{aligned}$$

in which the volumetric dilution rate, denoted by b, is defined by the undermentioned expression

$$b = \frac{X(\text{diluted } N_2 \text{ or } CO_2)}{X(O_2 \text{ in air})}. \tag{22}$$

By varying the dilution rate and the excess air, different flame regimes are encountered, namely, anchored stable

flames (flame NA in Fig. 9, flame CA in Fig. 10), A–L transient unstable flames (flame NB in Fig. 9, flame CB in Fig. 10), lifted stable flames (flame NC in Fig. 9, flame CC in Fig. 10), L–S transient unstable flames (flame ND in Fig. 9, flame CD in Fig. 10) and near-extinction stretched flames (flame NE in Fig. 9, flame CE in Fig. 10). The visualization of these representative flames are achieved by CH* imaging, from which the averaged flame images are obtained. In Figs. 9 and 10, the evolution of flame shapes and the corresponding stability domains are associated. A brief description of the observed flame regimes is provided as follows.

Anchored stable flame The flame is relatively short and exhibits a compact reaction zone. The anchorage on the edge of the swirl burner is observed.

A–L transient unstable flame With a slight increase in fluctuating light intensity, the flame becomes relatively unstable in comparison to the anchored flame. During the transition from anchored to lifted states, two separated CRZs appear shortly downstream the air–fuel injection. An extension of reaction zone along the tube wall is also observed.

Lifted stable flame The combustion process occurs far downstream the injection plane. The lean flame is stably lifted in the cylindrical chamber and exhibits a large and intense reaction zone, which indicates the flame restabilization. It should be noted that increasing air excess tends to move the reaction zone away from the burner, thus combustion does not occur anymore in the CRZ.

L–S transient unstable flame The transition from lifted to stretched states destabilize the flame. In a narrow equivalence ratio range the flame becomes very unstable in terms of intensity and position. Strong low-frequency oscillations of flames are identified both visually and acoustically.

Near-extinction stretched flame Before lean extinction, the flame takes a long stretched shape and gets anchored once again on the swirl burner. In this regime, the flame does not extend towards the near-wall regions, but remains in the central flow.

Globally, N_2-diluted methane flames and CO_2-diluted methane flames follow the same pattern evolution. Nonetheless, all the domains corresponding to five flame regimes described above are shifted to lower excess air (higher equivalence ratio) for CO_2-diluted flames. For example, the dilution rate is chosen at $b = 0.8$: for N_2-diluted flames, this dilution level corresponds to lifted sable flames; for CO_2-diluted flames, stretched flame regime is attained with this dilution rate. According to the previous study of Schefer *et al.*,[23] this trend can be linked to the decrease of the fuel laminar flame speed. In fact, higher laminar flame speed favors the burning at leaner conditions (higher excess air).

It is noticed that both N_2 dilution and CO_2 dilution affect the lean blow-out (LBO) limits negatively. The same example is taken ($b = 0.8$): the LBO limit of the N_2-diluted flames drops from 0.79 to 0.56, while that of the CO_2-diluted flames decreases from 0.79 to 0.4 (Fig. 11). The negative effect of dilution on LBO limits can be compensated by reactant preheating. Figure 11 points out that reactant preheating obviously broadens the flammability domain of the diluted flames. The measured LBO limits in preheating cases extend towards leaner conditions. Furthermore, CO_2 progressively disadvantage the flame stability in comparison to N_2 when increasing the dilution rate at fixed preheating temperature.

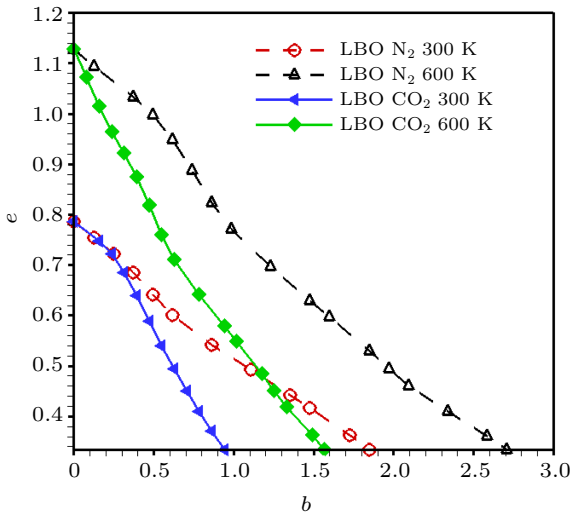


Fig. 11. (color online) Comparison of lean blow-out (LBO) limits between N_2 dilution 300 K, N_2 dilution 600 K, CO_2 dilution 300 K, and CO_2 dilution 600 K.

5. Dilution effects on flame structure with or without preheating

According to the preliminary results and discussion on the representative regimes of diluted flames, four series of five operating conditions are selected for further discussion on flame structure evolution and summarized in Tables 1–4. For all the cases, the excess air is kept constant ($e = 0.333$) so that the only factors taken into account is the dilution rate and initial temperature.

In order to discuss the dilution effects on flame structure, laminar flame speed, and laminar flame thickness should be calculated. As mentioned in Section 2.3, laminar flame speed and temperature distribution are computed by using Chemkin code. Then, we calculate the flame thickness δ_l based on the results of temperature distribution, applying the relation proposed by DeGoey *et al.*[24]

$$\delta_l = \frac{T_{(\nabla T)_{\max}} - T_u}{(\nabla T)_{\max}}. \tag{23}$$

The Karlovitz number can thus be estimated with the following expression:

$$Ka = \left(\frac{u'}{S_L^0}\right)^{\frac{3}{2}} \left(\frac{l_t}{\delta_l}\right)^{-\frac{1}{2}}, \tag{24}$$

where u' is the velocity fluctuation measured in a previous study using the same experimental configuration.[25] Integral length scale is estimated to be the diameter of the injector (18 mm) according to Aldredge *et al.*[26]

Table 1. Summary of operating conditions of N_2 dilution without preheating ($T = 300$ K, $P = 1$ atm, $e = 0.333$).

Flame	b	S_L^0/cm·s^{-1}	δ_l/mm	Ka	Re
NA	0.123	22.57	0.378	43	15242
NB	0.738	14.53	0.535	98	17071
NC	0.985	12.09	0.642	142	17833
ND	1.231	10.07	0.743	201	18557
NE	1.354	9.21	0.832	243	18928

Table 2. Summary of operating conditions of N_2 dilution with preheating ($T = 600$ K, $P = 1$ atm, $e = 0.333$).

Flame	b	S_L^0/cm·s^{-1}	δ_l/mm	Ka	Re
NPA	0.123	22.61	0.342	41	9221
NPB	0.738	14.54	0.515	96	10328
NPC	0.985	12.15	0.633	140	10789
NPD	1.231	10.11	0.729	198	11227
NPE	1.354	9.24	0.823	241	11457

Table 3. Summary of operating conditions of CO_2 dilution without preheating ($T = 300$ K, $P = 1$ atm, $e = 0.333$).

Flame	b	S_L^0/cm·s^{-1}	δ_l/mm	Ka	Re
CA	0.157	19.64	0.414	55	15585
CB	0.470	12.39	0.605	133	17071
CC	0.627	9.92	0.739	205	17833
CD	0.783	7.87	0.903	321	18557
CE	0.862	6.79	1.101	442	19548

Table 4. Summary of operating conditions of CO_2 dilution with preheating ($T = 600$ K, $P = 1$ atm, $e = 0.333$).

Flame	b	S_L^0/cm·s^{-1}	δ_l/mm	Ka	Re
CPA	0.157	19.68	0.407	54	9428
CPB	0.470	12.45	0.604	132	10328
CPC	0.627	9.94	0.727	203	10789
CPD	0.783	7.91	0.899	318	11227
CPE	0.862	6.82	1.092	437	11826

The Reynolds number (Re) is estimated by using bulk-flow properties in non-reacting conditions (preheating or non-preheating) of the incoming air flow and the internal diameter of the quartz combustion chamber. Although Re are different, e and b in the preheating cases (Tables 2 and 4) remain the same values as in the non preheating cases (Tables 1 and 3) in order to facilitate the comparison. It is emphasized that the flame regimes corresponding to the chosen operating conditions for the preheating cases are not necessarily similar to those discussed in Section 4, since the preheating impacts should be accounted for.

The results shown in Tables 1–4 indicate that the increase in dilution rate results in the decrease in laminar flame speed for both N_2 and CO_2, due to the degradation of the flame reactivity with the presence of diluting species. Meanwhile, flames are thickened by dilution. This dual effect of dilution leads to increasing values of the Ka number. Compared to N_2, the Ka number of CO_2-diluted flames is more sensitive to the variation in dilution rates. For example, the highest Ka number found to the most N_2 diluted flame at 300 K ($b = 1.354$) is 243, while that related to the most CO_2 diluted flame at 300 K ($b = 0.862$) reaches 442. Since the higher the Ka number, the more easily the turbulence can alter the flame structure. In this sense, the Ka number is considered as a dominant parameter for extinction behavior, which further confirms the dilution effects on LBO limits discussed in Section 4. However, the fact that reactant preheating could extend LBO limits to leaner conditions cannot be explained by the Ka number, since the Ka numbers calculated at the same dilution rate and different preheating temperatures are at the same level. For example, for flame NE (Table 1), $Ka = 243$; for flame NPE (Table 2), $Ka = 241$. Although reactants preheating is proved to increase the reactivity of the mixture and reduce the flame thickness (Tables 1–4), the variation of Ka number resulted from preheating is negligible. The Re number is more affected by the preheating temperature, and thus is more likely to be responsible for the extension of LBO limits observed at 600 K. For example, the Re number for flame NE ($T = 300$ K, $b = 1.354$, $Ka = 243$) is 18928, but the Re number for flame NPE ($T = 600$ K, $b = 1.354$, $Ka = 241$) drops to 11457. A decrease of 39.5% is attained with initial temperature varying from 300 K to 600 K. In fact, the augmentation in preheating temperature results in the reduction in Re number, leading to a decrease in turbulence intensity.

Another important aspect to evaluate the flame structure is the analysis on flame curvature distribution and its statistics. To achieve this, OH-PLIF measurements have been performed. The recorded PLIF images are processed appropriately using a conditioned level-set method[27] with block-division strategy to extract the flame contour. It is essential to smooth the contour edge before calculating the local curvature. For this purpose, a Savitsky–Golay algorithm[28] is employed, using a subroutine introduced by Press *et al.*[29] The value of the coefficients in this algorithm was derived from a least square fit of 13 neighboring points to a second-order polynomial function. Overall, large-scale flame wrinkling is well captured by the smoothed contours. Quantization noise and experimental errors of small scales are removed.

In this study, the curvature for each flame-front pixel is calculated using the following expression:[30]

$$H = \frac{\frac{\mathrm{d}y}{\mathrm{d}s}\frac{\mathrm{d}^2x}{\mathrm{d}s^2} - \frac{\mathrm{d}x}{\mathrm{d}s}\frac{\mathrm{d}^2y}{\mathrm{d}s^2}}{\left[\left(\frac{\mathrm{d}x}{\mathrm{d}s}\right)^2 + \left(\frac{\mathrm{d}y}{\mathrm{d}s}\right)^2\right]^{3/2}}, \tag{25}$$

where the curvature is defined to be positive when the flame-front is convex towards the reactants, x and y are Cartesian coordinates, and s is the parameterized curve curvilinear coordinate. Based on the imaging scaling of 12.1 pixels per mm, the maximum curvature that can be measured with less than 20% error is approximately 2 mm^{-1} which corresponds to a radius of 0.5 mm. The bounds of resolvable curvature were then set to be ± 2 mm^{-1}.

The calculated probability density functions for all the operating conditions (Tables 1–4) are illustrated in Fig. 12. It can be seen that all the probability density functions (PDFs) have a near-symmetric distribution with a near-zero mean. This general behavior is in good agreements with the majority of experimental data reported previously.[31–35] The results of other studies suggest that curvature PDFs are not particularly sensitive to variations in equivalence ratio.[36] This confirms our choice of operating conditions under investigation.

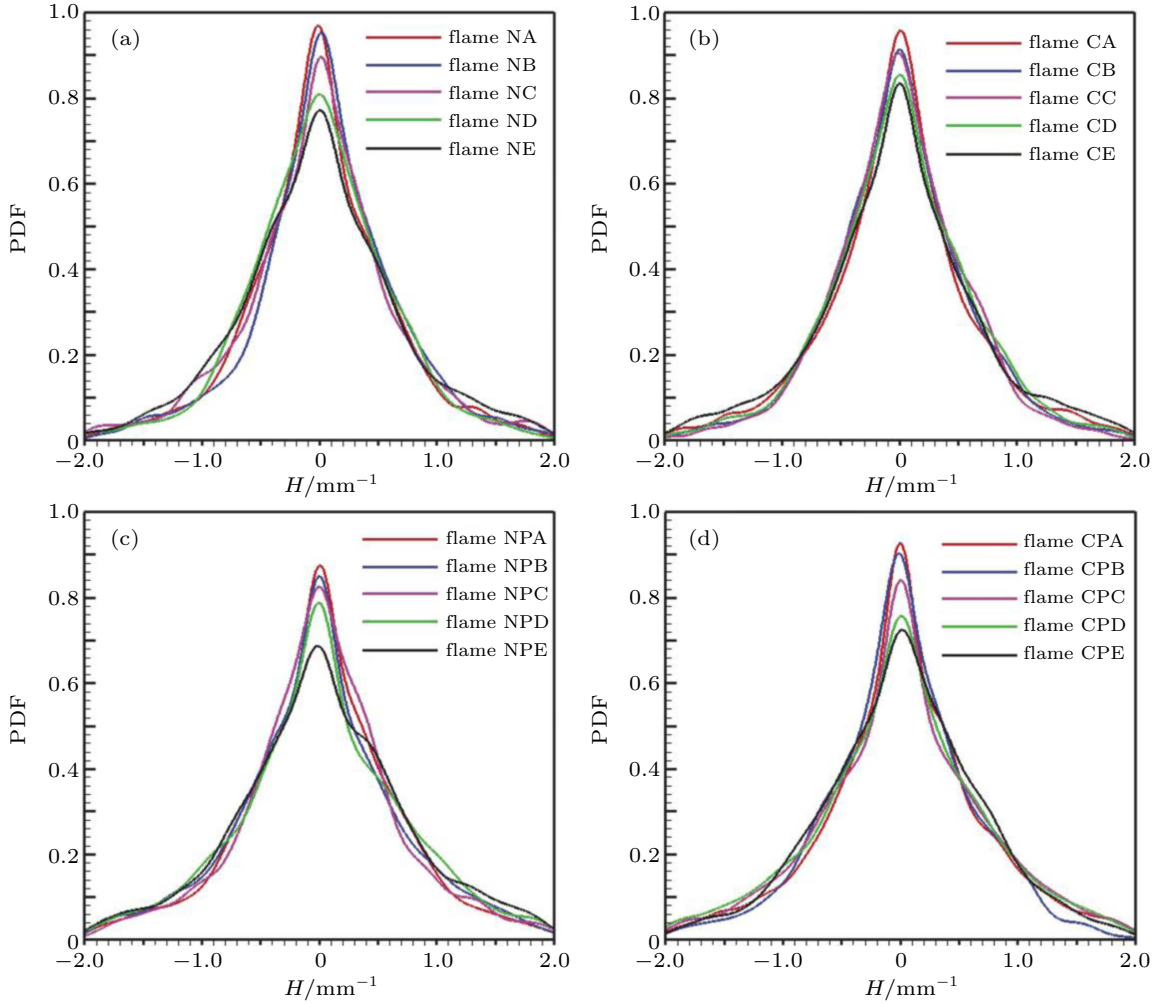


Fig. 12. (color online) Probability density functions of local curvature measured for different operating conditions: (a) N_2-diluted flames at 300 K; (b) CO_2-diluted flames at 300 K; (c) N_2-diluted flames at 600 K; (d) CO_2-diluted flames at 600 K.

To interpret the curvature shown in Fig. 12, the mean, standard deviation, skewness, and kurtosis of the curvature PDFs are calculated (Fig. 13) and plotted against the Reynolds number which is closely related to the turbulence intensity. The mean curvature is around zero and marginal positive at lower Re. As turbulent velocity fluctuations increase and become dominant, the PDFs become centered on zero. The increase in the standard deviation of the mean local curvature is brought about by an increase in the bulk Reynolds number for each individual case of operating conditions as expected.[31,32] Similar trends have been identified for premixed propagating flame kernels by Haq *et al.*[33] using OH-PLIF. It is found that the flames having similar values of Ka number exhibit similar behavior in terms of standard deviation. For example, flame NA ($Ka = 43$, $Re = 15242$), flame NPA ($Ka = 41$, $Re = 9221$), flame CA ($Ka = 55$, $Re = 15585$), and flame CPA ($Ka = 54$, $Re = 9428$): despite of the change in the Re number, the Ka number is almost at the same level; the SDs calculated for these flames have no remarkable differences. Consequently, the comparison among all the four datasets reveals that the Ka number effect is more significant than the Re number effect concerning the standard deviations. Gen-

erally symmetric Gaussian distributions with approximately zero skewness are encountered and justified by Fig. 13. The similar results were observed by Bonaldo and Kelman[34] for a weakly swirled burner using planar laser-induced Rayleigh scattering (LIRS), and Tanahashi *et al.*[35] for a confined axially swirled burner using simultaneous CH and OH-PLIF. All the PDFs have a kurtosis close to 3.5, indicating a peaky distribution. The kurtosis is found to decrease with increasing bulk Reynolds number for each case. Theoretically, PDFs should become increasing Gaussian with turbulence. In conclusion, all these factors deduced from PDF statistics support a trend towards a more Gaussian distribution with increasing bulk Reynolds number, provided that the initial temperature is invariant. When the reactants are preheated, SD and Kurtosis do not vary monotonously with *Re*, which implies that *Ka* number has dominating impacts.

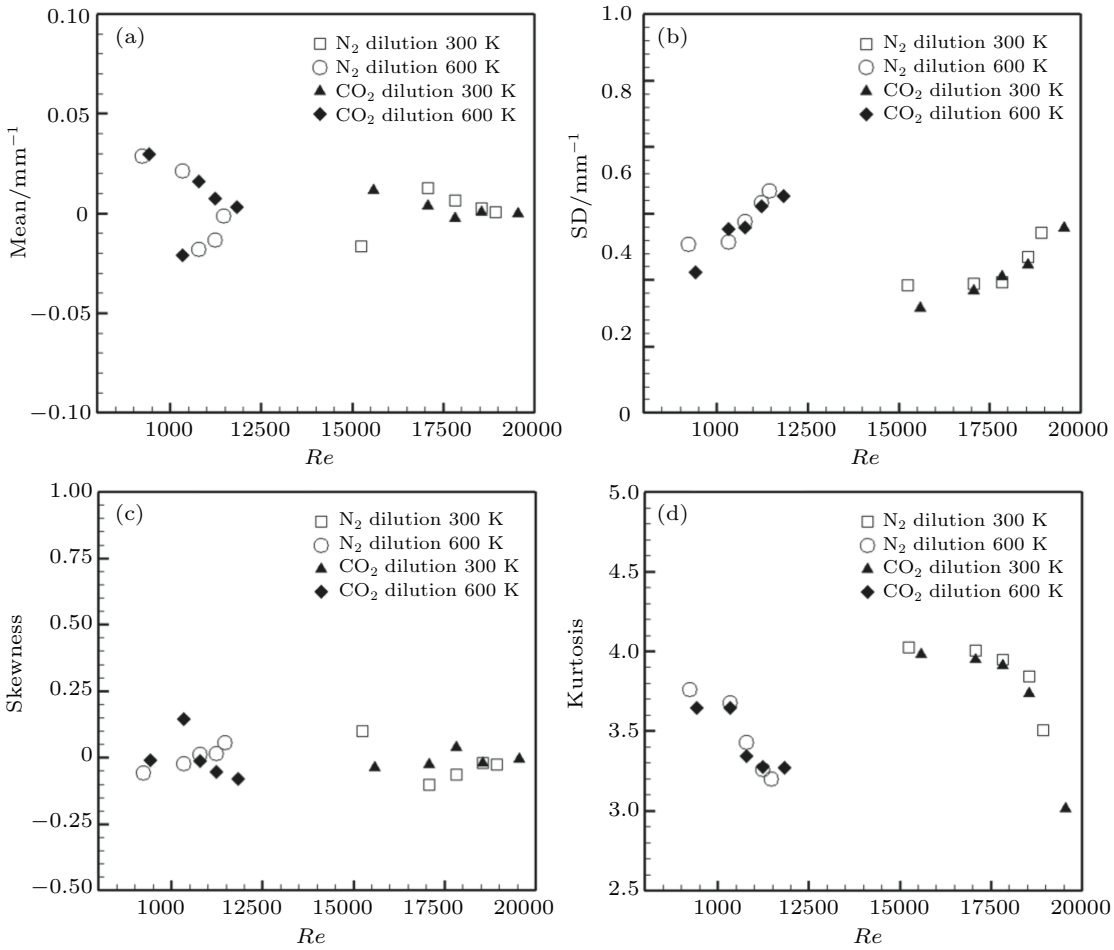


Fig. 13. Moments of the curvature PDFs (shown in Fig. 12) against Reynolds numbers: (a) mean; (b) standard deviation; (c) skewness; (d) kurtosis.

6. Dilution effects on pollutant emissions

The main purpose of adding diluting species into reactants is to achieve the reduction in pollutant emissions. This part of the study is dedicated to evaluating how dilution impacts pollutant emissions so as to assess their benefits and drawbacks.

Considering the change of dilution due to the variation of the equivalence ratio and the change of the fuel characteristics with the injection of diluents in the fuel mixture, pollutants emissions (x) are expressed (in units of mg/kWh) as

$$x\left(\frac{\text{mg}}{\text{kWh}}\right) = x^{\text{measured}}(\text{ppmv})\rho_x^{(\text{n})}\frac{V_{\text{F,Blend}}^{(\text{n})}}{\text{LHV}_{\text{Blend}}}, \qquad (26)$$

where $\text{LHV}_{\text{Blend}}$ is the low heating value of the blended fuel (in units of MJ/kg), $\rho_x^{(\text{n})}$ is the density of the studied pollutant (NO_x or CO), and $V_{\text{F,Blend}}^{(\text{n})}$ the volume of the dry combustion gases produced by 1 kg blended fuel. The exponent n indicates normal pressure and temperature conditions. The reproducibility of the measurements is less than 0.18 mg/kWh for both NO_x and CO emissions.

Firstly, it can be seen that the increase of excess air leads to substantial decrease of NO_x emissions at fixed dilution rates for both N_2 (Fig. 14) and CO_2 (Fig. 15). For example, when the N_2 dilution rate is set to 0.2 (Fig. 14), NO_x emissions are reduced from 5.7 mg/kWh ($e = 0.333$) to 2.8 mg/kWh ($e = 0.538$). At the same dilution rate ($b = 0.2$) for CO_2-diluted flames (Fig. 15), the reduction of NO_x emissions is even more significant: from 6.6 mg/kWh ($e = 0.333$)

to 2.5 mg/kWh ($e = 0.538$). It is known that thermal NO mechanism is directly linked to the adiabatic combustion temperature and is regarded as the main pathway of NO_x formation. High combustion temperature favors in particular the formation of thermal NO, and consequently low temperature limits the NO production. As a result, less NO is produced when the excess air is increased to attain fuel lean conditions, corresponding to lower combustion temperature.

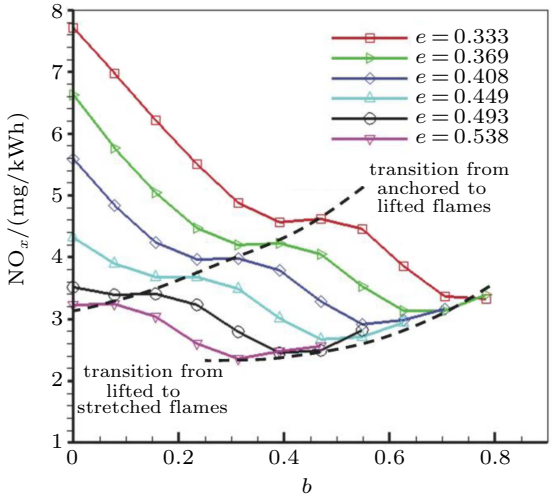


Fig. 14. (color online) NO_x emissions of N_2-diluted flames.

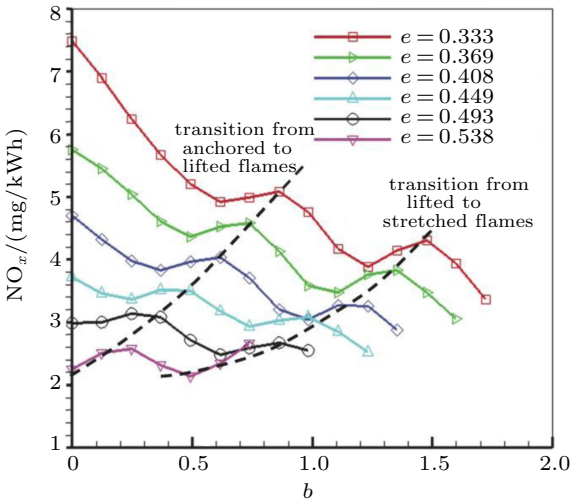


Fig. 15. (color online) NO_x emissions of CO_2-diluted flames.

Secondly, it is observed that dilution effects of N_2 and CO_2 on NO_x emissions are more obvious for fuel-rich conditions (for example, $e = 0.333$) than for fuel-lean conditions ($e = 0.538$). It can be concluded that dilution rate becomes the dominating parameter for NO_x reduction when excess air is low; combustion temperature plays a predominant role in reducing NO_x production when excess air is high. Nevertheless, for all the cases, the profiles of NO_x emissions are quite similar and repetitive. Great attempt has been made to correlate the NO_x emission profiles (Figs. 14 and 15) with flame stability diagrams (Figs. 9 and 10). NO_x emission profiles are in the wavelet form in the presence of two peaks. Thus, they are not monotone. Tracing back to flame stability diagrams, the values of e and b corresponding to the divisions between adjacent flame states can be noted and plotted in the NO_x emission profiles. By linking these plotted points, two curves can be obtained, which are approximately around the peaks. These two curves turn out to be related to 'transition from anchored to lifted flames' and 'transition from lifted to stretched flames', respectively. In fact, the transitional states of flames are temporarily unstable so that a slight increase in NO_x emissions will be caused by the combustion-induced thermoacoustic instability.[37]

The results on NO_x emissions are consistent with the fact that using lean premixed combustion to reduce NO_x production is a favored approach. Unfortunately, this approach is limited because the NO_x reduction obtained with lean combustion often induces increase in CO emissions due to local extinction. Contrary to NO_x emissions, CO emissions increase along with the excess air (Figs. 16 and 17). It is noteworthy that CO emissions of N_2-diluted flames (Fig. 16) are strongly increased compared to that of the CO_2-diluted flames (Fig. 17) because of the thermal dissociation. Maximums of CO emissions are noticed at LBO limits. This can be explained by the fact that the flames under near-extinction conditions became extremely unstable at that stage and the poor completeness resulted in high CO emissions.

The augmentation of N_2 or CO_2 dilution rate results in global reduction of NO_x emissions and increase of CO emissions. Although these two trends seem to be contradictory, optimal dilution rates can still be found to achieve an ideal compromise. For N_2-diluted flames (Figs. 14 and 16), optimal dilution rate is found to be comprised between 0.3 ($e = 0.538$) and 0.8 ($e = 0.333$); for CO_2-diluted flames (Figs. 15 and 17), optimal dilution rate varies from 0.1 ($e = 0.538$) to 0.5 ($e = 0.333$).

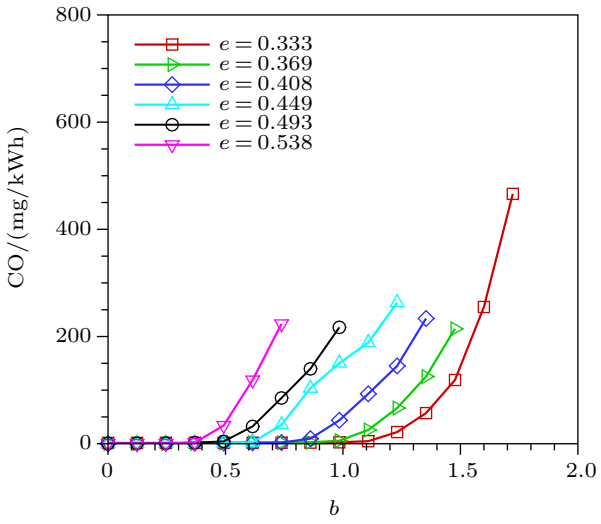


Fig. 16. (color online) CO emissions of N_2-diluted flames.

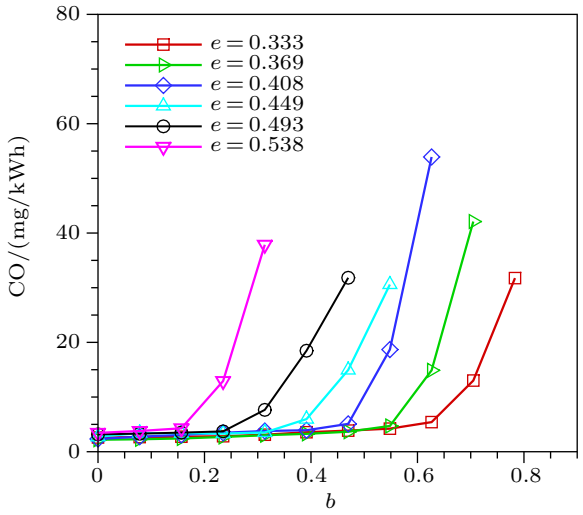


Fig. 17. (color online) CO emissions of CO_2-diluted flames.

7. Conclusions

The present study focuses on a systematic assessment of dilution effects on flame stability, flame structure and pollutant emissions of premixed methane–air flames. Two main diluting species, N_2 and CO_2, are taken into consideration. A numerically-aided experimental approach is adopted to investigate the combustion in diluted regimes. In numerical aspects, large eddy simulations are performed for non-reacting conditions in order to gain knowledge about cold flow topology and estimate aerodynamic swirl number; Chemkin calculations are carried out, giving access to the information about main parameters of flame characteristics, such as laminar flame speed, at various operating conditions. In experimental aspects, CH* chemiluminescence measurements are conducted to establish the stability diagrams of diluted flames; OH-PLIF measurements are achieved to discuss the dilution impacts on flame structure by means of statistical analysis on flame curvature distributions; pollutant emissions are evaluated using a multi-gas analyzer.

Although most industrial applications of combustion opt for a premixed configuration, problems on combustion instabilities due to premixing remain to be tackled. Flame stabilization through swirl motion is a viable solution. In this context, a swirl-stabilized combustion chamber is designed. Results on non-reacting flows prove the existence of the recirculation zones and thus validate the design.

According to CH* chemiluminescence results, five main flame regimes are observed with N_2 dilution: anchored stable flame, A–L transient unstable flame, lifted stable flame, L–S transient unstable flame and near-extinction stretched flame. CO_2-diluted flames follow the same pattern evolution, but the domains are shifted to lower excess air (higher equivalence ratio). Both N_2 dilution and CO_2 dilution affect the LBO limits negatively. However, the negative effect of dilution on LBO limits can be compensated by reactant preheating which broadens the flammability domain of the diluted flames. The measured LBO limits in preheating cases extend towards leaner conditions.

Dilution is found to have dual effects: the aerodynamic aspect is linked to *Re* number; the chemical and thermal aspect is related to *Ka* number. Preheating is supposed to have the same dual effects, since it results in reduction of *Re* number (aerodynamic aspect), increase of flame reactivity (chemical aspect), and decrease of flame thickness (thermal aspects). Most phenomena observed in the current study, in terms of flame stability and flame structure, can be explained by the competition between *Re* number and *Ka* number. In other words, it is of great importance to evaluate which one is the dominant factor for a given phenomenon.

Concerning the dilution effects on pollutant emissions, a correlation between NO_x emission profiles and flame stability diagram is established. Optimal dilution rates are estimated to achieve positive influence on both NO_x and CO emissions for the operating conditions under discussion.

This study is driven by the need for environmentally-friendly combustion approaches. The reported results serve to make contribution to the fundamental database of dilution effects on premixed methane/air flames. We have demonstrated the feasibility of adding N_2 and CO_2 as diluents in a swirl-stabilized combustor. This confirms the current industrial trends of applying biogas or EGR technology to achieve clean combustion.

Acknowledgments

The authors acknowledge the technical support from the CORIA Laboratory.

References

[1] Maruta K, Abe K, Hasegawa S, Maruyama S and Sato J 2007 *Proc. Combust. Inst.* **31** 1223
[2] Maruta K, Muso K, Takeda K and Niioka T 2000 *Proc. Combust. Inst.* **28** 2117
[3] Ishiguro T, Tsuge S, Furuhata T, Kitigawa K, Aral N, Hasegawa T, Tanaka R and Gupta A K 1998 *Proc. Combust. Inst.* **27** 3205
[4] Gupta A K, Bolz S and Hasegawa T 1999 *J. Energy Resour. Technol.* **121** 209
[5] Lille S, Dobski T and Blasiak W 2000 *J. Propul. Power* **16** 595
[6] Yuan J and Naruse I 1999 *Energy Fuels* **13** 99
[7] RØrtveit G J, Hustad J E, Li S C and Williams A 2002 *Combust. Flame* **130** 48
[8] Flamme M 2004 *Appl. Therm. Eng.* **24** 1551
[9] Galmiche B, Halter F, Foucher F and Dagaut P 2011 *Energy Fuels* **25** 948
[10] Chigier N A and Beér J M 1964 *J. Basic Eng.* **86** 788
[11] Davies T W and Beér J M 1971 *Proc. Combust. Inst.* **13** 631
[12] Beér J M and Chigier N A 1972 *Combustion Aerodynamics* (London: Elsevier) p. 138
[13] Syred N and Beér J M 1974 *Combust. Flame* **23** 143
[14] Gupta A K, Beér J M and Swithenbank J 1977 *Combust. Sci. Tech.* **17** 119

[15] Erlebacher G, Hussaini M Y, Speziale C G and Zang T A 1992 *J. Fluid Mech.* **238** 155

[16] Moin P and Kim J 1982 *J. Fluid Mech.* **118** 341

[17] Wang X W, Cai G B and Jin P 2010 *Chin. Phys. B* **19** 19401

[18] Dixon-Lewis G 1968 *Proc. Roy. Soc. A* **307** 111

[19] Smith G P, Golden D M, Frenklach M, Moriarty N W, Eiteneer B, Goldenberg M, Bowman C T, Hanson R K, Song S, Gardiner W C, Lissianski V V and Qin Z 1999 *GRI Mech 3.0*

[20] Broda J C, Seo S, Santoro R J, Shirattikar G and Yang V 1998 *Proc. Combust. Inst.* **27** 1849

[21] Gupta A K, Lilley D G and Syred N 1993 *Swirl Flows* (Cambridge: Abacus Press) p. 253

[22] Vanoverberghe K, van Den Bulck E and Tummers M 2004 *Flow Turbul. Combust.* **73** 25

[23] Schefer R W, Wicksall D M and Agrawal A K 2002 *Proc. Combust. Inst.* **29** 1131

[24] DeGoey L P H, Plessing T, Hermanns R T E and Peters N 2005 *Proc. Combust. Inst.* **30** 859

[25] Taupin B 2003 *Etude De La Combustion Turbulente A Faible Richesse Haute Temperature Et Haute Pression* (PhD thesis) (Rouen: INSA de Rouen) (in French)

[26] Aldredge R C 1997 *Int. Commun. Heat Mass Transfer* **24** 565

[27] Han Y, Yu N J, Dai J and Cai G B 2013 *Proceedings of the* 3*rd IEEE International Conference on Computer Science and Automation Engineering*, November 1–3, 2013, Guangzhou, China

[28] Savitzky A and Golay M J E 1964 *Anal. Chem.* **36** 1627

[29] Press W H, Teukolsky S A, Vetterling W T and Flannery B P 1992 *Numerical Recipes in Fortran* 77*: The art of Scientific Computing* (2nd edn.) (Cambridge: Cambridge University Press) p. 496

[30] Mokhtarian F and Mackworth A 1986 *IEEE Trans. Pattern Anal. Mach. Intell.* **8** 34

[31] Kostiuk L W, Shepherd I G and Bray K N C 1999 *Combust. Flame* **118** 129

[32] Ayoola B O, Balachandran R, Frank J H, Mastorakos E and Kaminski C F 2006 *Combust. Flame* **144** 1

[33] Haq M Z, Sheppard C G W, Woolley R, Greenhalgh D A and Lockett R D 2002 *Combust. Flame* **131** 1

[34] Bonaldo A and Kelman J B 2009 *Combust. Flame* **156** 750

[35] Tanahashi M, Murakami S, Choi G M, Fukuchi Y and Miyauchi T 2005 *Proc. Combust. Inst.* **30** 1665

[36] Lee T W, North G L and Santavicca A D 1993 *Combust. Flame* **93** 445

[37] Weigand P, Meier W, Duan X R and Aigner M 2006 *J. Eng. Gas Turbines Power* **129** 664